Dynamic dependence to domain wall propagation through artificial spin ice

D. M. Burn, M. Chadha, and W. R. Branford
Department of Physics, Imperial College London, London SW7 2BZ, United Kingdom
(Received 12 August 2016; revised manuscript received 27 February 2017; published 15 March 2017)

Domain wall propagation dynamics has been studied in nanostructured artificial kagome spin-ice structures. A stripline circuit has been used to provide localized pulsed magnetic fields within the artificial spin-ice (ASI) structure. This provides control of the system through electrically assisted domain wall nucleation events. Synchronization of the pulsed fields with additional global magnetic fields and the use of a focused magneto-optical Kerr effect magnetometer allows our experiments to probe the domain wall transit through an extended ASI structure. We find that the propagation distance depends on the driving field revealing field-driven properties of domain walls below their intrinsic nucleation field.

DOI: 10.1103/PhysRevB.95.104417

Magnetic metamaterials such as artificial spin ice show behavior arising from complex geometrical structuring in addition to the original material properties [1,2]. In these systems it is the combination of magnetic charge interactions and topological constraints that determine the magnetization behavior of the system. Artificial spin-ice structures consisting of arrays of magnetic nanobars provide a two-dimensional (2D) analog to explore frustrated magnetic phenomena [3,4]. These systems are of fundamental scientific interest [5–12] and have even been identified as potentials for novel neural network or processing technologies [3,13,14].

Magnetization reversal in artificial spin-ice structures composed of interconnected magnetic bars can be described by an ensemble of magnetic domain wall (DW) processes. The creation, annihilation, and propagation of these DWs throughout the system leads to magnetization reversal within the bars as well as the transport of both magnetic and topological charges throughout the system. The conservation of both magnetic and topological charge provides constraints on the creation and annihilation of DWs in the system. This reveals the physical significance of the finer details of the micromagnetic DW structure such as its chirality or topological makeup when the DW interacts with a complex magnetic structure [8,9,15–19].

The majority of our understanding of the magnetization behavior in artificial spin-ice systems is based on experiments combining thermal and quasistatic magnetic fields applied to the entire system [10,12,20–22]. The role of DWs has been typically investigated based on their natural occurrence [23], when an applied field exceeds the nucleation field. This is typically lower at the edges of the structures. This approach is therefore limited in that we can only investigate the internal behavior of the system once a process related to the edge of the system takes place.

In this investigation, the localized injection of DWs along the length of a lithographically patterned microstrip is employed [24,25]. Here, the pulsed-field DW injection technique allows control over the DW nucleation location within the system leading to significant experimental advantages as the DW nucleation process can be separated from a global applied field. First, this allows the behavior of DWs in the system to be investigated in a wider field range, even at lower fields than their nucleation field. Second, this allows the magnetization dynamics in the system to be explored. This is of great interest in the artificial spin-ice system, and understanding of the behavior in a dynamic context is necessary for any future technological applications. In this work we will outline current models for the propagation of DWs through artificial kagome spin-ice systems. This will be compared with experimental results where magnetization dynamics provides additional features which modify the predicted DW behavior in this system.

Our understanding of the propagation path of transverse DW through a series of vertex structures connected with thin narrow bars can be explained through topological considerations. Figure 1 shows a two-vertex section of an artificial spin-ice structure assumed to be within a continuous lattice, initially magnetized to the left and where the initial DW structure originated from the left. The arrows represent the magnetization orientation in each bar and with topological defects pinned to the edges of the structure associated with both the DWs and the vertices.

Figure 1 shows the evolution of a down-chirality DW incident upon a vertex with initial magnetization saturated to the left. During the interaction the $-\frac{1}{2}$ topological defect initially belonging to the DW becomes pinned on the upper edge of the vertex. The $+\frac{1}{2}$ from the DW follows the edge of the structuring and pairs with the $-\frac{1}{2}$ initially associated with the vertex. This new defect pair corresponds to a DW which is able to propagate along the lower branch at the vertex. The similar $+ve$ magnetic charges of the initial DW and the vertex provide a repulsive force which means there is an energy barrier associated with this process which can be overcome through the application of an applied magnetic field.

In Fig. 1(b), the $-ve$ charge of the second vertex now provides an attractive force on the positively charged DW. Here, the topological charges on the lower side of the nanobar are opposite and therefore unwind when they meet. The DW annihilates resulting in the two-in one-out state illustrated in Fig. 1(c) where just a $-\frac{1}{2}$ topological defect from the incident DW now remains pinned at the vertex. In this model, the DW no longer exists in the system.

Figure 1(d) shows how a new DW can be injected into the lower horizontal nanobar based on the state shown in Fig. 1(c). The lower edge of the vertex contains zero topological charge which is separated to form two defects of $+\frac{1}{2}$ and $-\frac{1}{2}$, respectively. The $+\frac{1}{2}$ forms a pair with the preexisting $-\frac{1}{2}$

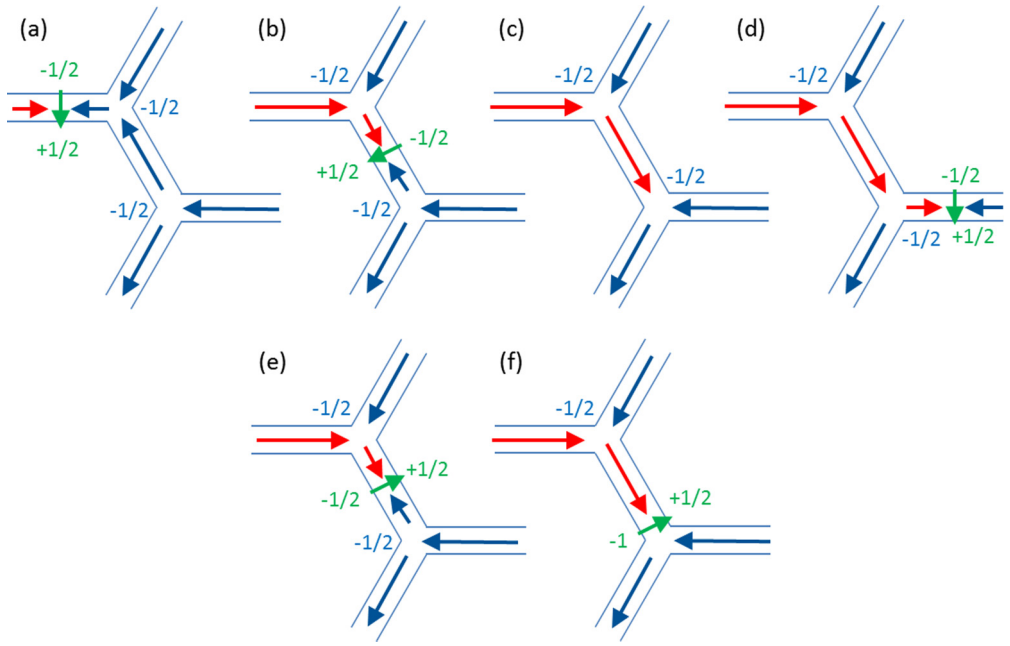

FIG. 1. Simple model of DW propagation and annihilation based on topological constraints in multiple vertices. The $\pm\frac{1}{2}$ and -1 labels indicate the topological edge defects associated with the DW (green) and vertex (blue).

defect on the upper edge of the vertex and represents a DW which can propagate along the nanobar, while the remaining $-\frac{1}{2}$ defect remains at the lower edge of the vertex. This process involves the separation of two opposite magnetic charges which gives rise to an energy barrier which needs to be overcome to complete this process.

The series of interactions illustrated in Figs. 1(a)–1(d) shows how an initial DW with down chirality can interact with two vertices in an artificial spin-ice structure resulting in a down-chirality DW in a subsequent nanobar with similar geometry. The repeat of this process is consistent with reversal events following from one another. A similar series of interactions would also take place for an up-chirality DW which would propagate along the upper branch at the first vertex. This would be followed by an equivalent annihilation event at the second vertex and the availability to nucleate a further up-chirality DW in the final horizontal nanobar. In all cases, a sizable magnetic field is required to supply the energy to overcome the energy barriers associated with moving like charges towards one another, and separating zero charge into a positive and negative charge pair.

With a greater applied field we expect dynamic DW processes to become apparent and have an influence upon the DW motion. For instance, when the applied field exceeds the Walker field, Walker breakdown will result in periodic transitions between the two transverse DW charalities via the traversal of the nanobar by an antivortex core. This core carries an integer topological charge between the edges of the nanobar allowing the topological edge charges to reverse their sign. A change in DW chirality in the horizontal bars in Fig. 1(a) would simply change the direction of propagation of the DW through the vertex similar to if an initial up-chirality DW wall was considered. However, if a reversal event occurs in the angled bars [Fig. 1(e)], its chirality is expected to become stabilized by the perpendicular field component [26], and the interaction between the DW and vertex is now different. Figure 1(f) shows a -1 topological defect is formed and this is not able to propagate through the vertex.

In this work, we experimentally probe the propagation length of DWs through a kagome artificial spin-ice system. We observe DW propagation over a significant distance below the nucleation field for DWs in this system. Also, this distance exhibits a driving field dependence. Both of these features are not predicted from our understanding based on the field-dependent manipulation of magnetic and topological charges combined with simplified behavior arising from Walker breakdown. Here, the field energy must overcome the energy barrier associated with DW nucleation for the DW to travel further than two bars.

By varying the bias field that drives DW motion, we investigate the importance of DW dynamics during propagation through an artificial spin-ice structure with the geometry of the applied field illustrated in Fig. 2. Combining localized DW injection with magneto-optical Kerr effect (MOKE) measurements with a localized magnetization probe, we also infer on the length scales of propagation through the system at these fields. Critically, our experiments probe the DW propagation behavior in fields below the intrinsic DW nucleation field for these structures.

Artificial spin-ice structures consisting of interconnected NiFe nanowires were fabricated in a kagome geometry using electron-beam lithography and thermal evaporation. The bars were 700 nm $\times$ 150 nm in dimension and were 10 nm thick. Further details about the patterning of the magnetic structures can be found elsewhere [27]. A 2-μm-wide Cr(5 nm)/Au(50 nm) microstrip was added in a second lithographic process and is shown in Fig. 2 along with the simulated field profile expected from the microstrip [28].

The magnetization reversal in the system was investigated using MOKE magnetometry in the longitudinal geometry.

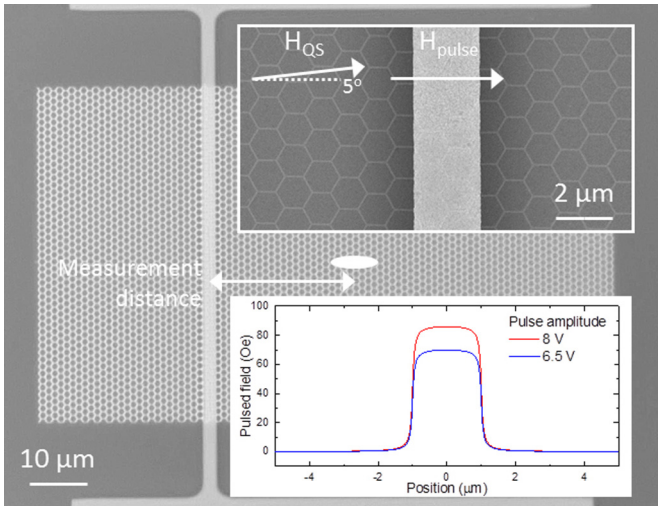

FIG. 2. Image of an interconnected array of nanowires with a Au stripline for applying localized pulsed magnetic fields. The geometry of the pulsed H_{pulse} and quasistatic H_{QS} fields is indicated with respect to the structuring. The ellipse indicates the position where measurements are made, a distance away from the stripline.

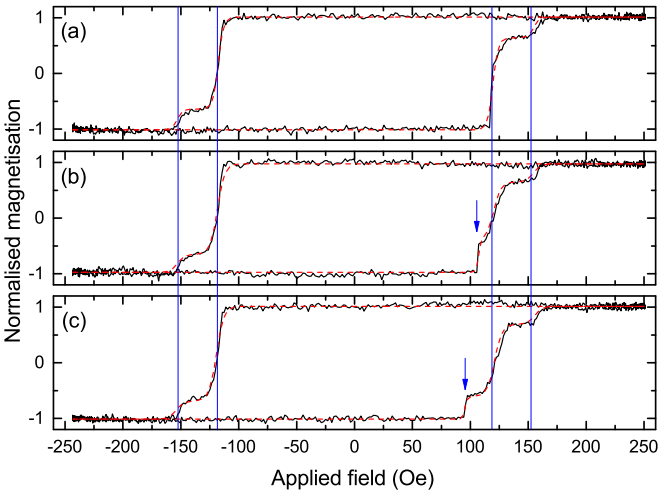

FIG. 3. MOKE hysteresis loops (black solid) showing the magnetization reversal driven by (a) a quasistatic magnetic field and (b) and (c) with the addition of a pulsed magnetic field with triggering indicated by the arrows. The loops show the behavior 9-V 20-ns pulses with the laser focused on top of the stripline. The fitted lines (red dashed) show a model fit to the data.

Here, a focused laser spot with a $\sim$10 μm elongated footprint provided a localized probe of the magnetization reversal as illustrated in Fig. 2. The combination of quasistatic and pulsed magnetic fields, supplied from external coils and from the microstrip, respectively, were used to drive the magnetization reversal in the sample. The Kerr signal was averaged over 50 field cycles in each measurement.

By introducing a 5° angular offset between artificial spin ice (ASI) structuring and the applied field direction, the magnetization reversal associated with DW nucleation events and DW propagation through the system can be distinguished by the reversal field [27]. Additionally, by varying the contribution from the quasistatic and pulsed fields, behavior from quasistatic energy-dependent magnetization reversal processes and time-dependent magnetization processes have been investigated [24,29].

Initially, the magnetization behavior was investigated with a 1-Hz sinusoidal quasistatic magnetic field and is shown in Fig. 3(a). Two transitions in the magnetization occur at two distinct and relatively sharp reversal fields despite averaging over 50 field cycles and over multiple nanowires within the illuminated laser footprint. The two steps indicate the combination of two reversal processes occurring during the magnetization reversal associated with the nucleation field of a DW from a vertex and the field required for a preexisting DW to propagate through a vertex [27].

By introducing additional pulsed magnetic fields with sub-ns rise times, Figs. 3(b) and 3(c) show modified hysteresis loops where the arrows indicate the triggering of the pulsed field within the quasistatic field cycle resulting in an increase in the magnetization. At this point, the combination of pulsed and quasistatic fields locally overcome the reversal field leading to the injection of magnetic DWs at the stripline. The additional pulsed-field-induced reversal results in a reduced magnetization reversal at the lower quasistatic field and the higher field quasistatic reversal remains unchanged.

The magnetization reversal combines multiple reversal processes which can be modeled as a summation of tanh functions [30]. The lines in Fig. 3 show a model fit to the data where each transition is parametrized by a reversal field, the relative change in magnetization, and a parameter representing the shape of that transition. The quasistatic reversal fields are symmetric with increasing and decreasing field and share fitting parameters.

The shape of the hysteresis loop step representing the increase in magnetization at the lower reversal field also shows some broadening when a pulsed field is present. This could represent a modified reversal field due to a partially reversed magnetization state following the pulse. This will be discussed in more detail later.

The pulsed-field-induced magnetization reversal depends on both the pulsed-field voltage and the triggering point within the quasistatic field cycle. Figure 4(a) shows the minimum pulse voltage required to result in the additional pulsed-field-induced magnetization reversal steps in Figs. 3(b) and 3(c). This is plotted as a function of the quasistatic field at the point of pulsed-field triggering which can be considered as a static bias field on the time scales of the pulsed field. The linear decrease represents the contributions to the total field at the stripline where an increase in pulsed-field amplitude from a greater pulsed voltage allows magnetization reversal to take place at a lower quasistatic field. A linear fit to these data provides a calibration of the stripline which produces 10.8 ± 0.3 Oe/V. For quasistatic fields greater than 122 Oe, the magnetization reversal is driven purely by the quasistatic field. Therefore, the effect of the pulsed field in this field regime cannot be distinguished.

Figure 4(a) also compares the difference in behavior when the laser spot is positioned 0, 10, and 20 μm away from the stripline. All the points fall on the same line, indicating the reversal process at the stripline is not affected by the

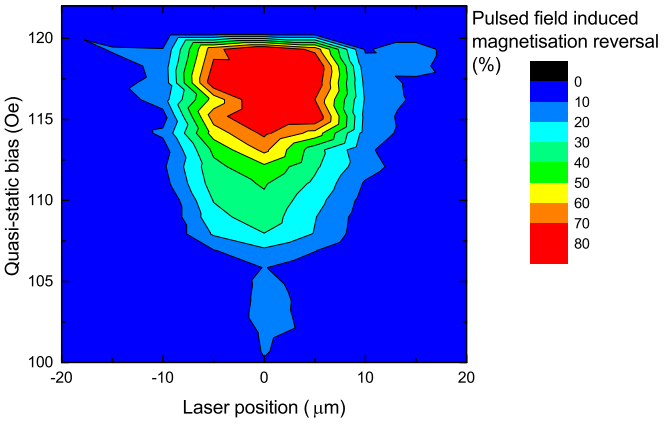

FIG. 4. Pulsed-field-induced magnetization reversal measured as a function of quasistatic bias field and measurement position from the stripline. 20-ns pulses at 7.5 V.

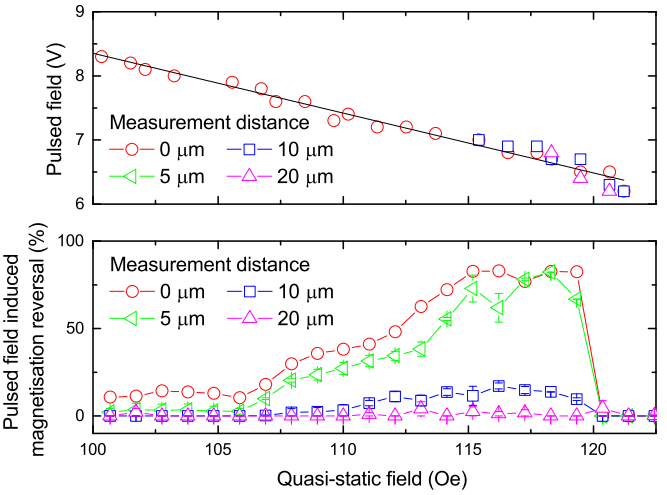

FIG. 5. (a) Minimum pulsed voltage required to lead to magnetization reversal when pulses are triggered at different quasistatic bias fields. (b) Pulsed-field-induced magnetization reversal as a function of quasistatic bias field measured at various distances from the DW injection stripline. Pulses are 20 ns and 7.5 V.

measurement position. However, when measurements are performed at a greater distance from the stripline, magnetization reversal is only observed when the pulsed-field triggering occurs at larger quasistatic fields. This feature allows us to probe the motion of the DWs through an extended region of the ASI system.

For all measurement positions, the combination of pulsed and quasistatic fields still results in magnetization reversal at the stripline. This reversal is due to the localized injection of magnetic DWs at the stripline which propagate along the nanobars reversing the magnetization near the stripline. At greater distances from the stripline only the quasistatic field drives the DW propagation and the magnetization reversal represents the dynamic behavior of DWs at this field, which is below the DW nucleation field.

Pulse lengths of 150 and 20 ns had little influence on the DW injection process, so the quasistatic bias field dependence on DW propagation has been further investigated with 20 ns long. Also, 7.5-V pulses were chosen which are sufficient to inject DWs when biased with a field greater than 108 Oe. Figure 4(b) shows the pulsed-field-induced magnetization reversal contribution as a function of the quasistatic bias field for various measurement positions. This is found from the ratio in magnetization change from the pulsed and quasistatic fields in the hysteresis loops.

Measurements at the stripline location show a large pulsed-field-induced magnetization change which is most significant when a large quasistatic field is used to drive the DW propagation. Here, the result represents DWs which reverse the magnetization in nanobars near where they are nucleated.

When the quasistatic bias field is reduced below 115 Oe, the magnetization change decreases. This indicates that the proportion of pulsed-field-induced reversal events within the region probed by the laser spot is reduced. This can be explained by DWs which are not able to propagate so far through the structure in the lower fields.

Measurements at greater distances from the stripline show magnetization reversal driven purely by the quasistatic field (see field profiles in Fig. 2). Here, a lower magnetization change is found as injected DWs must propagate through a greater number of nanobars and vertices before reaching the probed region. This means that DW pinning is more likely, but at high quasistatic bias fields, DW propagation up to 15 μm is still observed.

The DW propagation distance through the structure is more clearly shown in in Fig. 5 where the pulsed-field-induced magnetization reversal is plotted as a function of the measurement position and the quasistatic field. Here, a strong reversal is centered around the position of the stripline at 0 μm which becomes more significant with greater quasistatic fields. Again, as the fields approach 120 Oe, the pulsed-field-induced reversal becomes indistinguishable from the quasistatic field driven reversal.

With the large quasistatic fields, the distance over which the reversal can be detected is much greater than for the smaller quasistatic fields resulting in a triangular shape in Fig. 5. This shows how the propagation of a DW through the artificial spin-ice structure depends on the driving field applied to the DW. With low fields the propagation distance is limited as multiple nanobars and interconnecting vertices are encountered and provide pinning sites. However, with greater fields the pinning from these become less significant allowing the DW propagation over a greater number of nanobars and vertices.

The simplified model illustrated in Figs. 1(a)–1(d) shows the behavior of a DW in the system based on quasistatic energy considerations of the system. Here, a DW is constrained to travel along only two bars of the system until a field in excess of the nucleation field allows for the nucleation of another DW. Even with transitions in DW chirality from Walker breakdown the DWs are expected to become pinned as illustrated in Figs. 1(e) and 1(f). Our experimental results demonstrate the propagation of a DW over a greater distance of the artificial spin-ice structure in fields below this nucleation field. Additionally the DWs are able to propagate with a driving field dependence to their propagation length in the system.

The propagation at a reduced field can be explained by considering the energy embodied by the incident propagating

DW. The DW micromagnetic structure leads to an increase in exchange and demagnetization energies above that of the empty bar. When propagating in a field this is also modified by the Zeeman energy contribution. Between Figs. 1(b) and 1(c), the energy associated with the DW is released as it is annihilated. This energy is typically radiated in the form of spin waves but may also assist with the nucleation of a secondary DW shown in Fig. 1(d). This additional energy would mean less Zeeman energy is required for the nucleation from an external driving field. This modification to the energetics of the nucleation process may also be affected by the local spin configuration at the vertex resulting from the arrival of the dynamically propagating DW. The spins will not be in their energetically minimized configuration, which is also likely to perturb the energy barrier needed for the nucleation of the secondary domain wall.

For high driving fields, other features in addition to the changing chirality of the DW from Walker breakdown should also be considered. Additional effects such as the change in internal micromagnetic structure emission and absorption of energy in the form of spin waves and the reciprocating motion of a DW during Walker breakdown are other features known to affect DW motion with high driving fields. The change in chirality requires an antivortex structure to traverse the width of the bars, effectively transferring an integer amount of topological charge between the edges of the bar. Possibilities may also exist for integer topological charge to be transported over a vertex which may remove the topological constraints giving only a two-bar DW propagation limit that has been discussed earlier.

The propagation length dependence can also be explained in terms of the energetics of the dynamically propagating DWs. With a greater quasistatic driving field, the DWs have a greater Zeeman energy contribution. Even though the micromagnetic structural rearrangement within the DW tries to reduce the total energy, the total energy with applied field is greater. This means that the DWs can encounter, and overcome, a greater number energy barriers associated with the vertices before becoming pinned. The lower-energy DWs become pinned after fewer vertices and therefore travel a reduced distance through the artificial spin-ice structuring.

In conclusion, we have probed the magnetization reversal in artificial spin-ice systems experimentally through focused MOKE magnetometry. The combination of pulsed and quasistatic magnetic fields allow for the injection of DWs and the study of their dynamic interactions with the geometrical structuring for a range of DW driving fields. Our results demonstrate control over the location of injected DWs within artificial spin-ice structures and how DW propagation distance depends on the external driving field.

Existing quasistatic models based on the manipulation of magnetic and topological charges throughout the system do not account for propagation beyond two bars for fields below the nucleation field. Our experimental results demonstrate propagation beyond this limit which has been attributed to the release of energy stored within the micromagnetic structure of a DW and modifications to the energy barrier for a incident dynamic DW. Upon annihilation, the energy from the DW is used to assist the nucleation of a second DW at the vertex, enabling its formation below the intrinsic nucleation field. Variations in propagation distance arise for DWs propagating under different driving fields. This difference has also been linked to variations in the energy stored within the micromagnetic structure of a DW which varies in the dynamic regime. Additionally, in the case of a DW driven at high field in the Walker regime, the possibility of integer topologocial defect transitions through the system has been considered which may lift the topological constraints in this regime.

This work was supported by the Engineering and Physical Sciences Research Council (Grant No. EP/G004765/1) and the Leverhulme Trust (Grant No. RPG 2012-692).

Data statement: Data requests should be addressed to dataenquiryexss@imperial.ac.uk

[1] C. Nisoli, R. Moessner, and P. Schiffer, Rev. Mod. Phys. **85**, 1473 (2013).

[2] L. J. Heyderman and R. L. Stamps, J. Phys.: Condens. Matter **25**, 363201 (2013).

[3] R. F. Wang, C. Nisoli, R. S. Freitas, J. Li, W. McConville, B. J. Cooley, M. S. Lund, N. Samarth, C. Leighton, V. H. Crespi, and P. Schiffer, Nature (London) **439**, 303 (2006).

[4] E. Mengotti, L. J. Heyderman, A. F. Rodríguez, F. Nolting, R. V. Hügli, and H. B. Braun, Nat. Phys. **7**, 68 (2010).

[5] S. Ladak, D. E. Read, G. K. Perkins, L. F. Cohen, and W. R. Branford, Nat. Phys. **6**, 359 (2010).

[6] R. V. Hügli, G. Duff, B. O'Conchuir, E. Mengotti, A. F. Rodríguez, F. Nolting, L. J. Heyderman, and H. B. Braun, Philos. Trans. A **370**, 5767 (2012).

[7] A. Farhan, P. M. Derlet, A. Kleibert, A. Balan, R. V. Chopdekar, M. Wyss, J. Perron, A. Scholl, F. Nolting, and L. J. Heyderman, Phys. Rev. Lett. **111**, 057204 (2013).

[8] W. R. Branford, S. Ladak, D. E. Read, K. Zeissler, and L. F. Cohen, Science **335**, 1597 (2012).

[9] N. Rougemaille, F. Montaigne, B. Canals, M. Hehn, H. Riahi, D. Lacour, and J. C. Toussaint, New J. Phys. **15**, 035026 (2013).

[10] Y. Qi, T. Brintlinger, and J. Cumings, Phys. Rev. B **77**, 094418 (2008).

[11] S. Zhang, I. Gilbert, C. Nisoli, G.-W. Chern, M. J. Erickson, L. O'Brien, C. Leighton, P. E. Lammert, V. H. Crespi, and P. Schiffer, Nature (London) **500**, 553 (2013).

[12] U. B. Arnalds, A. Farhan, R. V. Chopdekar, V. Kapaklis, A. Balan, E. T. Papaioannou, M. Ahlberg, F. Nolting, L. J. Heyderman, and B. Hjörvarsson, Appl. Phys. Lett. **101**, 112404 (2012).

[13] S. Ladak, D. E. Read, T. Tyliszczak, W. R. Branford, and L. F. Cohen, New J. Phys. **13**, 023023 (2011).

[14] P. E. Lammert, X. Ke, J. Li, C. Nisoli, D. M. Garand, V. H. Crespi, and P. Schiffer, Nat. Phys. **6**, 786 (2010).

[15] S. A. Daunheimer, O. Petrova, O. Tchernyshyov, and J. Cumings, Phys. Rev. Lett. **107**, 167201 (2011).

[16] O. Tchernyshyov and G.-W. Chern, Phys. Rev. Lett. **95**, 197204 (2005).

[17] A. Pushp, T. Phung, C. Rettner, B. P. Hughes, S.-H. Yang, L. Thomas, and S. S. P. Parkin, Nat. Phys. **9**, 505 (2013).
[18] S. K. Walton, K. Zeissler, D. M. Burn, S. Ladak, D. E. Read, T. Tyliszczak, L. F. Cohen, and W. R. Branford, New J. Phys. **17**, 013054 (2015).
[19] P. Mellado, O. Petrova, Y. Shen, and O. Tchernyshyov, Phys. Rev. Lett. **105**, 187206 (2010).
[20] F. Montaigne, D. Lacour, I. A. Chioar, N. Rougemaille, D. Louis, S. Mc Murtry, H. Riahi, B. S. Burgos, T. O. Mente, A. Locatelli, B. Canals, and M. Hehn, Sci. Rep. **4**, 5702 (2014).
[21] Z. Budrikis, J. P. Morgan, J. Akerman, A. Stein, P. Politi, S. Langridge, C. H. Marrows, and R. L. Stamps, Phys. Rev. Lett. **109**, 037203 (2012).
[22] C. Nisoli, J. Li, X. Ke, D. Garand, P. Schiffer, and V. H. Crespi, Phys. Rev. Lett. **105**, 047205 (2010).
[23] S. Ladak, S. K. Walton, K. Zeissler, T. Tyliszczak, D. E. Read, W. R. Branford, and L. F. Cohen, New J. Phys. **14**, 045010 (2012).
[24] M. Hayashi, L. Thomas, Y. B. Bazaliy, C. Rettner, R. Moriya, X. Jiang, and S. S. P. Parkin, Phys. Rev. Lett. **96**, 197207 (2006).
[25] A. Himeno, T. Ono, S. Nasu, K. Shigeto, K. Mibu, and T. Shinjo, J. Appl. Phys. **93**, 8430 (2003).
[26] M. T. Bryan, T. Schrefl, D. Atkinson, and D. A. Allwood, J. Appl. Phys. **103**, 073906 (2008)
[27] D. M. Burn, M. Chadha, and W. R. Branford, Phys. Rev. B **92**, 214425 (2015).
[28] T. J. Silva, C. S. Lee, T. M. Crawford, and C. T. Rogers, J. Appl. Phys. **85**, 7849 (1999).
[29] D. M. Burn, E. Arac, and D. Atkinson, Phys. Rev. B **88**, 104422 (2013).
[30] B. K. Middleton, M. M. Aziz, and J. J. Miles, IEEE Trans. Magn. **36**, 404 (2000).